Evolution of CFRP stress cracks observed by *in-situ* X-ray refractive imaging

IOP Conf. Series: Materials Science and Engineering **942** (2020) 012035 doi:10.1088/1757-899X/942/1/012035

Evolution of CFRP stress cracks observed by *in-situ* X-ray refractive imaging

A Kupsch[1]*, V Trappe[1], B R Müller[1], and G Bruno[1,2]

[1] BAM Federal Institute for Materials Research and Testing, 12200 Berlin, Germany
[2] University of Potsdam, Institute of Physics and Astronomy, 14476 Potsdam, Germany

* E-mail: andreas.kupsch@bam.de

Abstract. Modern air-liners and wind turbine rotor blades are made up primarily of fiber reinforced plastics. Failure of these materials heavily impairs the serviceability and the operational safety. Consequently, knowledge of the failure behavior under static and cyclic loads is of great interest to estimate the operational strength and to compare the performance of different materials. Ideally, the damage evolution under operational load is determined with *in-situ* non-destructive testing techniques. Here, we report *in-situ* synchrotron X-ray imaging of tensile stress induced cracks in carbon fiber reinforced plastics due to inter-fiber failure. An in-house designed compact tensile testing machine with a load range up to 15 kN was integrated into the beamline. Since conventional radiographs do not reveal sufficient contrast to distinguish cracks due to inter-fiber failure and micro cracking from fiber bundles, the Diffraction Enhanced Imaging (DEI) technique is applied in order to separate primary and scattered (refracted) radiation by means of an analyzer crystal. This technique allows fast measurements over large fields-of-view and is ideal for *in-situ* investigations. Imaging and the tensile test are run at the highest possible frame rate (0.7 s^{-1}) and the lowest possible strain rate ($5.5 \cdot 10^{-4}$ s^{-1}). For 0°/90° non-crimp fabrics, the first inter-fiber cracks occur at 380 MPa (strain 0.8 %). Prior to failure at about 760 MPa (strain 2.0 %), we observe the evolution of nearly equidistant (1 mm distance) cracks running across the entire sample in the fully damaged state.

1. Introduction

Fiber reinforced plastics, FRPs, reinforced with carbon fibers or glass fibers, are polyvalent: they are an established material in aircraft construction, they are widely used in wind turbine rotor blades and increasingly used in automotive engineering. The low weight together with the high strength make this class of materials very attractive for modern lightweight construction applications. In general, FRPs are of increasing interest for structural components in lightweight constructions, whose failure wholly or partially impairs serviceability and operational safety.

Knowledge of the spatial and temporal evolution of cracks is valuable for both the manufacturer and the customer of composite materials in order to estimate the material's lifetime. In the case of transparent glass fiber reinforced plastics (GFRP), the behavior prior to and during fracture has been successfully recorded by common optical systems with mega-pixel resolution [1, 2]. While the occurrence of the first cracks in GFRPs can be inspected with visible light, it is not suited to characterize the evolution of micro cracks at high load levels or due to cyclic loading. Since the (integral) intensity of transmitted light is not proportional to the internal surface per volume caused by micro cracks, the number of cracks has to

be evaluated by image analysis [3, 4]. Additionally, the increasing intensity of transmitted light due to increasing crack opening at a constant number of cracks can be mistaken for increased inner surface.

In a comparative study, the inter-fiber failure in GFRP has been investigated by means of X-ray-refraction topography [5, 6]. This technique overcomes the disadvantages of visible light absorption techniques, depending on the type and size of cracks. Separated cracks could be imaged, and the internal (specific) surface was determined by calculating the co-called X-ray refraction value [5]. Even dry textiles or impregnated laminate can be quantitatively analyzed with this technique, for instance for different mean fiber filament diameters even at identical fiber volume content.

2. Experimental

2.1. Samples

The CFRP specimens were made from 2 layers of a 400 g/m² twill style textile and 4 layers of a 200 g/m² NCF, each made with Tenax-E HTA40 E1, 6K yarn (400tex) (figure 1). In both cases the stacking sequence was symmetric and balanced. In the non-crimp fabric, the carbon fiber rovings were fixed by a 34tex glass fiber yarn. The matrix system used was Huntsman Araldite® LY 556 / Aradur® 917 / Accelerator DY 070. Carbon fiber reinforced plastics, CFRP, plates were manufactured in a resin transfer moulding technique, and flat specimens with a length of 140 mm, a width of 10 mm (0°/90°-laminate and -45°/+45°-laminate) and a thickness of 1.1 mm were cut out and tested. Tab reinforcement was applied onto the 0°/90°-specimens for clamping. Due to the high Poisson's ratio of the -45°/+45°-laminate, the fracture occurs in the middle of the specimens even without the tabs. 0°/90°- and -45°/+45°-laminates of each textile reinforcement were investigated. The fiber volume content is 41% in both laminates.

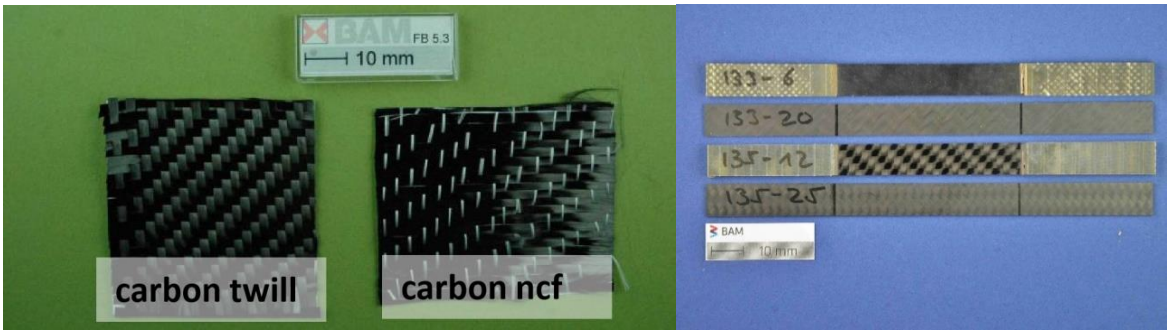

Figure 1. Carbon twill and carbon NCF textiles used for the specimen preparation (left) and photograph of the produced specimens (right): NCF (top two) and twill (bottom two). Specimens with 0°/90° fiber orientation were additionally prepared with tab reinforcements.

Table 1. Compilation of the fabrics investigated. The specimen names are assigned to the type of fabrics and fiber orientation relative to the direction of tensile stress.

	0°/90°	-45°/+45°
non-crimp fabric (NCF)	133-3, 133-11	133-17, 133-19
2 × 2 twill fabric (TF)	135-10, 135-14	135-18

2.2. X-ray refraction

X-ray refraction techniques were introduced a few decades ago [7] and have been successfully used for both material characterization and non-destructive testing [8]. These techniques are used to obtain the amount of the relative internal specific surface (*i.e.*, surface per unit volume, relative to a reference state) of a specimen, and are therefore effective in the investigation of inhomogeneities within fiber reinforced plastics such as cracks, fibers, and fiber debonding.

X-ray refraction occurs whenever X-rays interact with interfaces between materials of different density, as in the case of cracks, pores, and particles in a material. This is analogous to the behavior of

visible light in transparent materials, such as lenses or prisms. It should be noted that the X-ray refraction index is smaller than unity. Thus, the optical behavior is inverted [9], so structures such as pores act rather as focusing objects. The difference in the refraction indices between the two interfacing materials, the so-called refraction decrement, determines the refraction angle at the interface (angle between the propagation direction of the primary and the refracted beam). Since the refraction decrement for X-rays is of the order of 10^{-7} to 10^{-5}, X-ray optical effects can only be observed at very small deflection angles ranging from a few seconds to a few minutes of arc. X-ray refraction techniques detect pores and cracks as soon as they exceed a certain size or opening of a few X-ray wavelengths. Since the typical X-ray wavelengths are approximately 0.1 nm, the smallest detectable object size is down to the nanometer range. This is not to be confused with the spatial resolution or the size of the objects that can be *imaged*. The spatial resolution of the technique is limited by the pixel size of the detector system.

It must be emphasized that, because of the inevitable background noise, it is impossible to conclusively detect one single defect. A certain population of objects is necessary to yield an integrated signal above the background noise. Thus, X-ray refraction is primarily used in radiographic mode with thin specimens (platelets) and yields 2.5D information about the microstructure of the sample (*i.e.*, integrated over the whole specimen thickness); the 2D lateral resolution corresponds to the number and size of the detector pixels. This results in the detection and imaging of a population of defects and not in the imaging of single defects. If the lateral size of defects or structures exceeds the spatial resolution of the detector system, they can be localized by the X-ray refraction contrast. This analysis can be conducted on samples of macroscopic size of a few cm, where the field of view of X-ray refraction techniques is much larger than that of high-resolution X-ray computed tomography and of classic scanning electron or even optical microscopy. Furthermore, X-ray refraction techniques are sensitive to defect orientation, thereby allowing different kinds of defects to be identified. The refraction signal of an isotropic inhomogeneity, such as spherical voids, is present at any orientation of the specimen. For cracks or elongated pores, on the other hand, the signal decreases when the defect surface normal is parallel to the scattering vector of the detection system (the bisectrix between the incident and the refracted beam directions). The X-ray refraction signal has been *quantitatively* correlated to microstructural changes, which have been rationalized in micromechanical models [10-17].

2.3. X-ray refraction radiography by Diffraction Enhanced Imaging

Synchrotron X-ray refraction radiography (XRRR) measurements were carried out at the BAM synchrotron laboratory BAM*line* at the Helmholtz-Zentrum Berlin, Germany [18, 19]. A double crystal (Si (111)) monochromator (DCM) was used to extract a highly collimated monochromatic X-ray beam with an energy band width of 0.2 %. The beam energy was set to 25 keV. A flat panel detector in combination with a lens system and a 50 µm thick CWO scintillator screen provided a pixel size of 7.2 × 7.2 µm^2, capturing a field of view of about 14 × 7.2 mm^2. The incident beam was narrowed to the field of view by a slit system in order to avoid detector backlighting [20, 21]. The exposure time for each image was 1 second (plus 0.4 s read out time). In order to achieve a sufficient count rate per pixel we applied a 4 × 4 pixel binning, resulting in an effective pixel size of 28.8 × 28.8 µm^2. The X-ray beam was oriented along the specimen thickness direction (t = 1.1 mm).

In contrast to transmission-based radiographic measurements, a Si (111) analyzer single crystal was placed in the beam path between the specimen and the camera system, shown in figure 2a, to perform refraction radiographs (Diffraction Enhanced Imaging, [22]) in two different modes. In mode 1 the crystal is positioned in the X-ray beam in such a manner that the Bragg condition is fulfilled (Bragg angle θ_B = 4.537° at 25 keV, between beam direction and crystal surface) and the free X-ray beam (without sample) is completely reflected to the detector. In mode 2 the crystal is slightly tilted (by some 10^{-4}°), the Bragg condition is not fulfilled for the primary radiation. Here, we show images obtained in mode 1, exclusively. X-rays, refracted by the sample's internal surface such as cracks violate the Bragg condition. Hence, they are not reflected and create an additional attenuation to the sample's true absorption properties.

We performed complementary experiments with the samples 133-11 and 135-14 in mode 2, which revealed the same material behavior as their sister samples 133-3 and 135-10. In mode 2, only those beam portions are reflected by the analyzer, which fulfill the *actual* Bragg condition. The different contrasts are shown in figures 2b and 3.

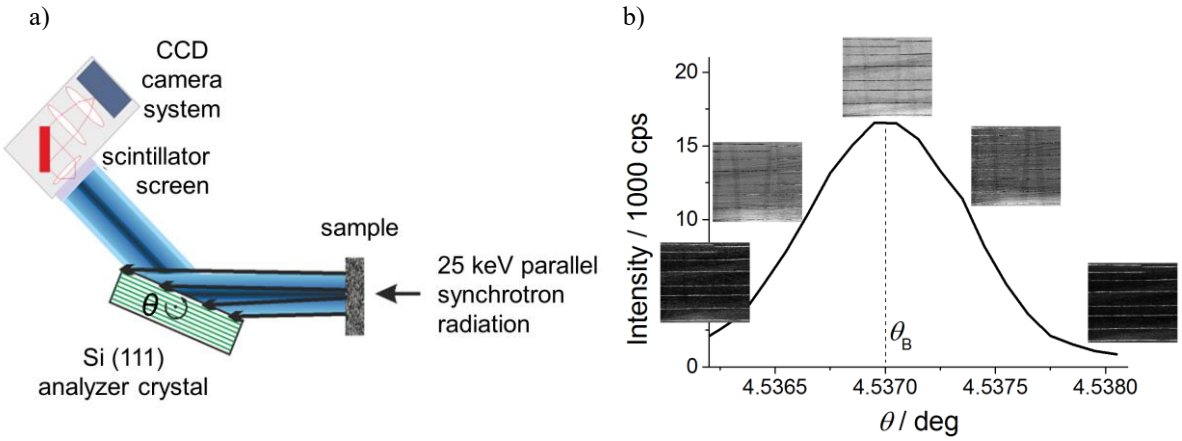

Figure 2. (a) Set-up of synchrotron X-ray refraction radiography. In the sketch, the dark shaded (attenuated) primary beam portions are diffracted by the analyzer crystal. The black arrowed rays (scattered by the sample) do not fulfill the Bragg condition, and thus are not reflected by the crystal (and not detected by the camera system). (b) The crystal's rocking curve provides X-ray images of changing contrast. In the center of the rocking curve (mode 1), all refracting beam portions are discarded and the primary beam is imaged, only. Thus, the cracks appear dark (low intensity). Off the center (mode 2), the primary beam is discarded. Only rays of a predefined refraction angle are accepted; the cracks appear as bright (high intensity) features.

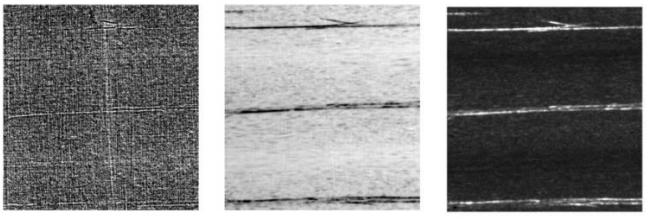

Figure 3. Comparison of absorption (left) and refraction contrast of a pre-loaded NCF CFRP sample ($(\sigma_{max}$=530 MPa). The middle image is obtained from the rocking curve center, the right image from an off-center rocking curve position.

2.4. In-situ tensile tests

A tensile rig with an electro-mechanical actuator and a hydraulic clamping system was integrated into the DEI set-up at BAM*line* (figure 4a). The compact load rig was designed and manufactured specifically for *in-situ* tensile and cyclic loading in a laboratory X-refraction set-up. The maximum load capacity is +/-15 kN. In the laboratory set-up, the loading of the FRPs must be performed in load steps, since each scan of the specimen takes more than one hour. At BAM*line*, the tensile tests were done with a typical actuator speed of 2 mm/minute, as is common in quasi static tensile tests standards [23]. The typical stress strain curves obtained during the tests are shown in figures 4b and 4c. Table 2 summarizes some mechanical characteristics of the individual samples (obtained from tensile testing).

Imaging and the tensile test were started separately. Roughly 15 seconds after continuous imaging had started, the tensile stress machine was set into displacement-controlled mode. It recorded the displacement (strain) and the applied force as a function of time. With the known time stamp, the single images were assigned to the respective stress/strain by computing residual images (figure 5a), *i.e.*, the difference of subsequent images. The variance of these residual images clearly indicated the start of the tensile test and the rupture (figure 5b). It should be noted that the generated cracks are clearly visible in the residual images, but their local contribution to the variance of the full image is too low to cause significant changes.

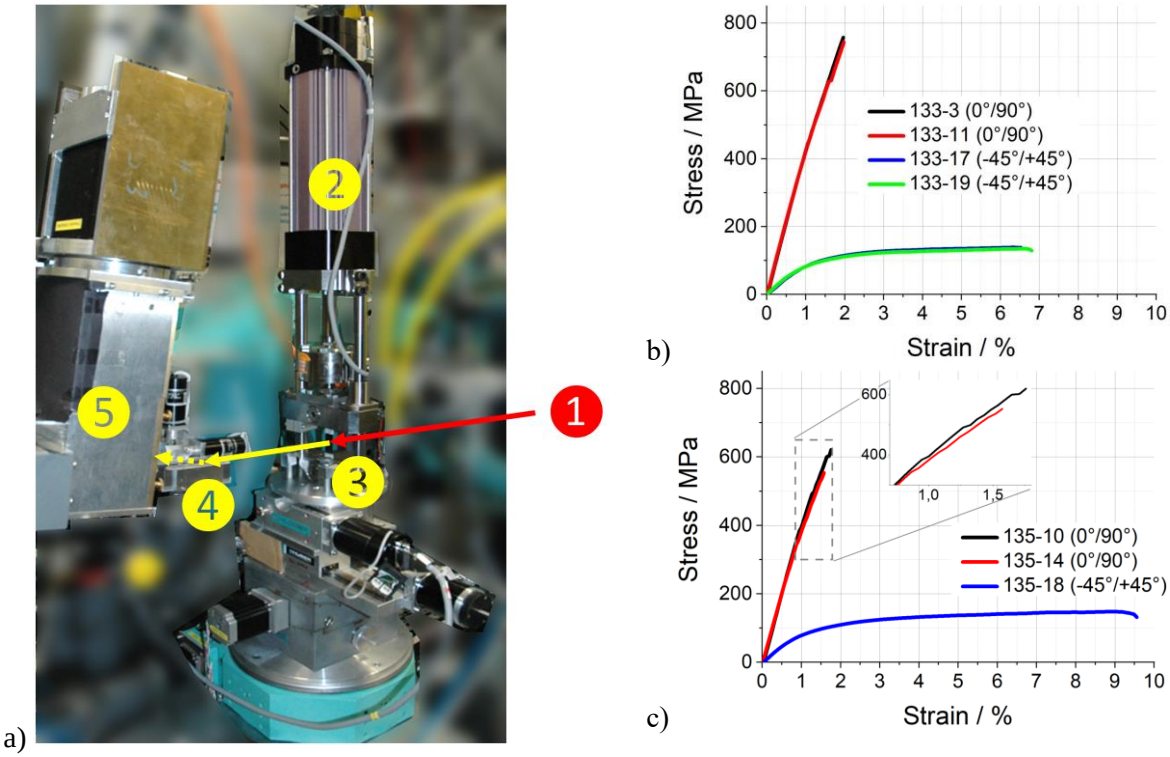

Figure 4. (a) Main components of the experimental set-up - The primary beam (red arrow) is emitted from (1) the synchrotron source and monochromatized by a DCM. It is absorbed and scattered by (3) the (loaded) sample; the tensile rig, including the electro-mechanical actuator, the load cell, and (2) the hydraulic clamping . The transmitted and scattered beam (solid yellow arrow) is diffracted at the analyzer crystal (4). The diffracted beam (dotted yellow arrow) is recorded by (5) the flat panel detector. Stress strain curves (b) of the non-crimp fabrics and (c) the twill fabrics reveal the larger stiffness of the NCF samples. The magnified detail in (c) visualizes the occurrence of transverse cracking and its impact on the slight decrease of the 0°/90° samples' stiffness ("Puck's knee" [24]).

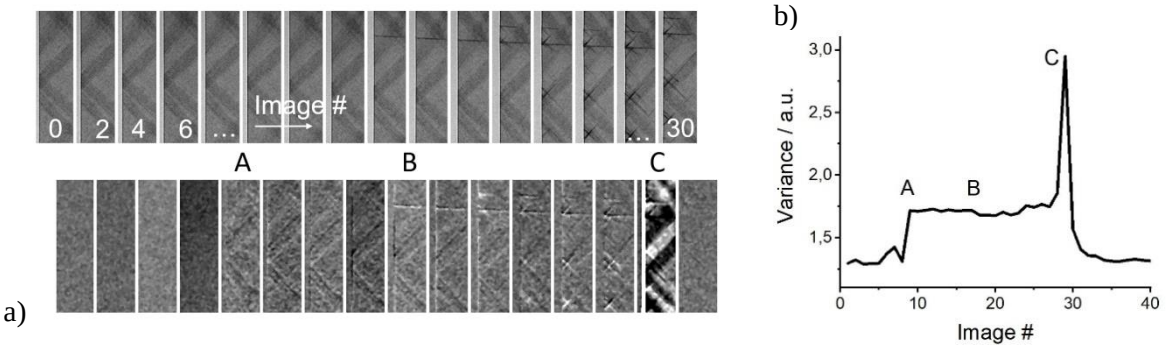

Figure 5. (a) Subsequent synchronization of imaging and tensile test with the example of an image detail of a -45°/+45° non-crimp fabric (sample 133-17). The as-measured radiographs (top row) are used to compute residual radiographs (bottom row). Points A, B, and C indicate the start of the tensile test, the appearance of first cracks, and the sample rupture, respectively. (b) Computing the variance of the residual radiographs reveals clear indication of A and C, while the evidence of B is less pronounced.

Table 2: Compilation of the tensile test results, where *UTS* is the ultimate tensile strength, ε_r the strain at rupture, and *E* is Young's modulus.

sample	type	Fiber orientation	*UTS* / MPa	ε_r / %	*E* / GPa
133-3	NCF	0°/90°	760	2.0	44.5
133-11	NCF	0°/90°	740	2.0	44.4
133-17	NCF	-45°/+45°	138	6.3	9.7
133-19	NCF	-45°/+45°	135	6.6	9.8
135-10	twill	0°/90°	620	1.8	41.2
135-14	twill	0°/90°	550	1.6	41.4
135-18	twill	-45°/+45°	148	8.9	9.6

3. Results

3.1. Non-crimp fabrics

Figure 6 shows selected images of the tensile test on the 0°/90° non-crimp fabric (specimen 133-3). Since the specimens are unnotched and the field of view is about 10% of the specimen's free length, it is a coincidence if the rupture occurs within the image.

The 35tex glass fiber binding yarn is not detectable by naked eye inspection (figure 1) when impregnated with the epoxy matrix. However, the density of the glass (ρ = 2.55 g/cm³) is significantly higher than the carbon fiber epoxy (according to fiber volume content of 41 % - ρ = 1.4 g/cm³). Hence, the glass fiber yarn causes an absorption contrast. Due to the orientation sensitivity of X-ray refraction, the contrast of the horizontal glass fiber yarns is enhanced compared to the perpendicular-oriented ones (absorption and refraction confounded *vs.* pure absorption). The specimens strain becomes visible by the displacement of the binding yarns.

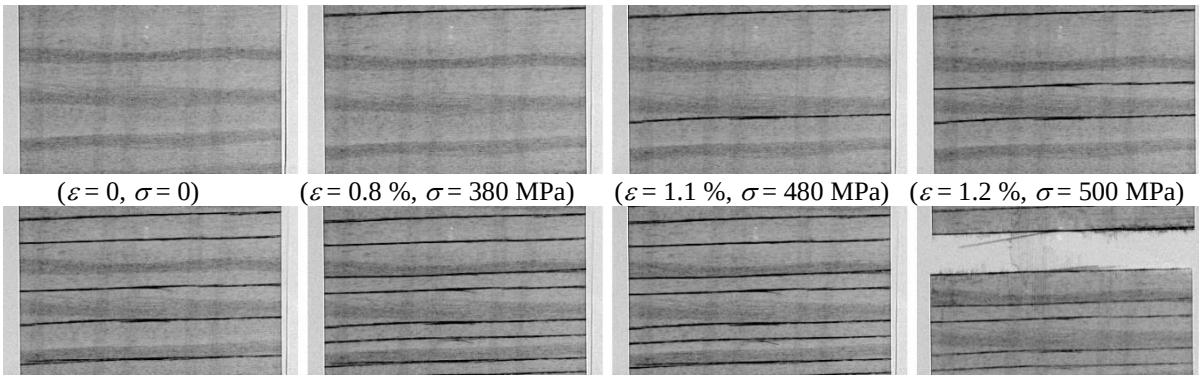

Figure 6. Selected XRRR images of the tensile test of the NCF sample 133-3 covering the start of the test, the subsequent occurrence of 90° inter-fiber cracks until reaching a saturated crack density, followed by rupture. The images correspond to a size of 11 × 7.2 mm². The respective strain (ε) and stress (σ) is indicated below each image.

Before the first cracks appear (σ = 380 MPa), the strain is evidenced from stretching the glass fiber yarns (figure 5a). The sample roughly follows a linear-elastic stress-strain behavior (Young's modulus 44.4 GPa [23]). However, due to the increasing number of transverse cracks, the stiffness of the specimen decreases slightly to a secant modulus of about 38 GPa short before rupture. Only 90° inter-fiber cracks are observed. Once such cracks are generated, they immediately cross the entire width of the NCF sample. (The time resolution does not allow locating the site of initiation.) In an intermediate state, they form an irregular pattern of 1 mm and 2 mm distance. Since subsequent cracks fill the 2 mm gaps symmetrically, before rupture (which is by chance in the field of view) we observe a regular 1 mm distance pattern, which corresponds to the saturated crack density for quasi static loading [2]. The

transverse strain is negligible. After the rupture due to 0°-fiber failure, the cracks remain visible with lower contrast, indicating reduced crack opening due the relaxed external load. However as discussed above, a transverse crack opening of a few nm is sufficient to generate the refraction contrast. A second measurement on specimen 133-11 (cf. figure 4b, table 1) confirmed the results obtained for 133-3.

Figure 7 shows selected images of the tensile test on the -45°/+45° non-crimped fabric (sample 133-17). Again, before the first cracks appear (at 123 MPa) the strain is evidenced from the stretching of the glass fiber yarns. Here, however, the translation of the yarn (due to displacement) is accompanied by fiber rotation by about 2° (figure 8a), which is due to the high Poisson's ratio (of about 0.7). The -45°/+45° NCF laminate shows a non-linear viscoelastic-plastic stress-strain behavior [1] (Young's modulus 9.7 GPa [23]) due to the strong influence of the polymer matrix up to the rupture strain (of about 6.3 %). Figure 8b demonstrates that the local remaining plastic deformation in the field of view is rather low.

The initial cracks observed are 90° cracks near the free edges and cross about 10 % of the sample width. Presumably, such cracks are generated in the matrix at the intersection of fiber bundles, where the epoxy matrix agglomerates. At higher strain (about 5 %), the generation of 45° inter-fiber cracks sets in; such cracks stop near the specimen's edges. Until rupture, we observe no cracks crossing the entire width of the sample in the field of view. A second measurement on sample 133-19 (cf. figure 4b, table 1) confirmed the results obtained on 133-17 but it shows that one particular 45° crack crosses the entire width at rupture in the field of view.

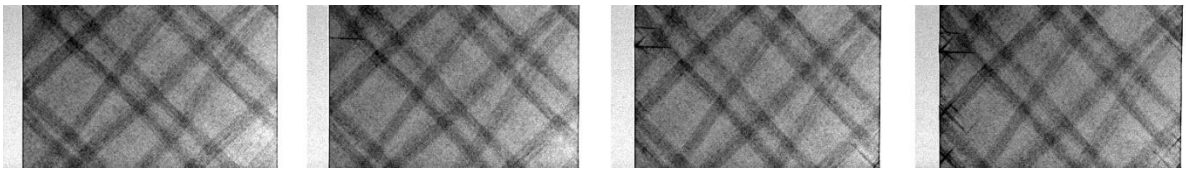

($\varepsilon = 0$, $\sigma = 0$) ($\varepsilon = 2.5$ %, $\sigma = 123$ MPa) ($\varepsilon = 4.9$ %, $\sigma = 135$ MPa) ($\varepsilon = 6.3$ %, $\sigma = 138$ MPa)

Figure 7. Selected XRRR images of the tensile test of the NCF sample 133-17 showing the start of the test, the first 90° crack, the first 45° inter-fiber cracks and the damage before rupture.

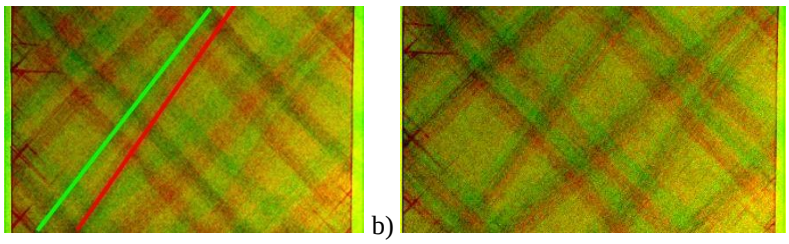

a) b)

Figure 8. (a) Fiber rotation of 2° visualized by the glass fiber yarns. The color image is composed of single XRRR images at the start of the tensile test (green picture) and short before rupture (red picture). The two solid lines indicate the translation and rotation of one and the same yarn in the two states. The light green areas on both sides of the sample indicate the transverse contraction (of about 5 %). (b) The low plastic deformation is evidenced by superimposing the start of the tensile test (green) with the image after rupture (red). The glass fiber yarns rotate back to their initial orientation, and the transverse contraction is nearly reversed (2 % residual contraction) in the field of view.

3.2. Twill fabrics

Figure 9 shows selected images of a 0°/90°-twill specimen (133-10) under tensile load. The slight horizontal whitening comes from the horizontal carbon fiber bundles and is due to the refraction contrast. The perpendicular fibers are not detectable [5, 6]. The first crack occurs at 340 MPa in the center of a fiber bundle. Subsequent cracks are also generated within the fiber bundles, where the local fiber volume is high. In contrast to the NCF-laminate, the cracks do not suddenly cross the total specimen width due to the presence of the perpendicular woven fiber bundles. With increasing load, about half of the cracks grow across the entire sample width. The crack density in the saturated state is lower than in the NCF-

laminate. However, in the roughly linear-elastic stress-strain behavior, the stiffness slightly decreases with the increasing transverse cracking by about 15 % to 35 GPa (detail in figure 4c), as observed with the NCF 0°/90° laminate. Finally, the twill textile shows a more damage tolerant inter-fiber failure behavior accompanied by a slightly lower total strength and stiffness compared to the NCF-textile. It should be noted that in this particular case, the stress-strain curve shows at least three "Puck knees" [24], *i.e.*, discontinuities, at about 400, 500, and 600 MPa. These kinks are a footprint of the occurrence of transverse cracks crossing the sample as the sample's compliance increases.

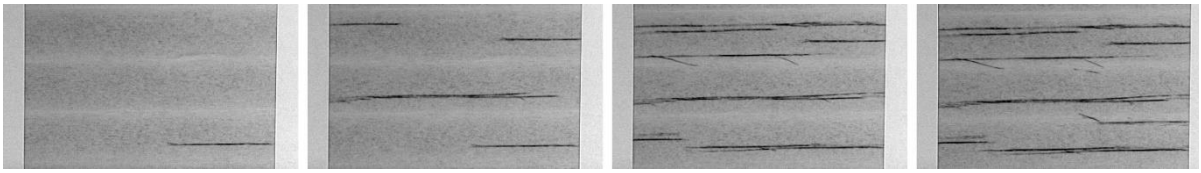

(ε = 0.8 %, σ = 340 MPa) (ε = 1.0 %, σ = 420 MPa) (ε = 1.4 %, σ = 520 MPa) (ε = 1.8 %, σ = 620 MPa)

Figure 9. Selected XRRR images of the tensile test of the twill sample 135-10 showing the first 90° crack, the first crack crossing the sample width, and the crack pattern at 520 MPa, which remains nearly unchanged until rupture at 620 MPa.

Cracking in the -45°/+45° twill specimen (figure 10, sample 135-18) starts at about 5% strain. The first cracks observed are 45° inter-fiber shear cracks of limited length at the free edges. With increasing load, 90°-cracks are generated in matrix-rich areas near the edges, preferably, at the intersections of former 45° cracks. However, they do not cross the entire sample width until rupture. The total crack density is low compared to the 0°/90°-laminates. In the -45°/+45°-twill-laminate, the refraction effect occurs in both fiber orientations (proportional to $1\text{-}\cos^2\alpha$, where α is the angle of fibers relative to the scattering direction, here: vertical [5]). Hence, the -45°/+45°-fiber bundles become visible.

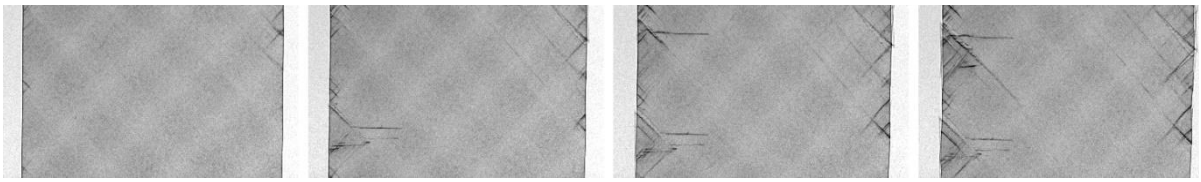

(ε = 5.0 %, σ = 137 MPa) (ε = 6.6 %, σ = 142 MPa) (ε = 8.9 %, σ = 148 MPa) (ε = 9.5 %, σ = 131 MPa)

Figure 10. Selected XRRR images of the tensile test of the twill sample 135-18, showing the first 45° inter-fiber cracks, the first 90° crack, and a grown crack pattern, which remains nearly unchanged until rupture at 131 MPa.

4. Conclusions

We have tracked the crack evolution in differently prepared carbon fiber reinforced plastics (CFRPs) by *in-situ* X-ray refraction imaging without the need to use contrast agents. The different samples showed significantly different mechanical behavior mainly due to fiber orientation: 0°/90° oriented fabrics show a linear elastic behavior and break at about 2 % strain, while -45°/+45° oriented ones show a viscoelastic-plastic behavior and break at considerably higher strain. It could be shown that crack generation is correlated to discontinuities in the stress-strain curves for 0°/90° samples. Crack generation and growth is mainly governed by the type of fabric: in non-crimp fabric (NCF) several cracks propagate across the sample, while twills stop cracks with the presence of perpendicular yarns. Hence, twill fabrics exhibit a lower strength and stiffness but higher damage tolerance. The comparatively low stiffness of the 0°/90° fabrics is due to the low fiber volume content of 41 %. The observed inter-fiber-failure is qualitatively similar to the phenomena observed with glass fiber reinforced plastics, GFRP. The cracks remain visible after the rupture, although at reduced contrast. This demonstrates that XRRR is sensitive even to cracks of very small opening, which are not detectable using X-ray absorption techniques at comparable spatial resolution.

Acknowledgements
The authors are indebted to T. Wolk, R. Britzke, S. Hickmann, and M. Harwardt (BAM) for assistance with the measurements. V.T. gratefully acknowledges financial support by the Deutsche Forschungsgemeinschaft (DFG) in the Priority Program 1466 "Life∞" under grant numbers TR499/3-1 and TR499/3-2.

References
[1] Trappe V and Harbich K W 2006 *Int. J. Fatique* **28** 1187.
[2] Müller A, Trappe V, Hickmann S and Ortwein H P 2018 Investigation of the infinite life of fibre-reinforced plastics using X-ray refraction topography for the *in-situ*, nondestructive evaluation of micro-structural degradation *Fatigue of Materials at Very High Numbers of Loading Cycles* ed. H J Christ (Wiesbaden: Springer Spektrum) pp. 417-439.
[3] Adam T J and Horst P 2018 Very high cycle fatigue testing and behavior of GFRP cross and angle-ply laminates *Fatigue of Materials at Very High Numbers of Loading Cycles* ed. H J Christ (Wiesbaden: Springer Spektrum) pp. 511-532.
[4] Adden S and Horst P 2006 *Compos. Sci. Technol.* **66** 626.
[5] Trappe V, Hickmann S and Sturm H 2008 *Mater. Test.* **50** 615.
[6] Trappe V, Hentschel M P and Ivers H 2006 *Proc. 16th Europ. Conf. of Fracture (Alexandroupolis)* (New York: Springer) p. 900.
[7] Hentschel, M P, Hosemann R, Lange A, Uther B and Brückner R 1987 *Acta Cryst*. A **43** 506.
[8] Müller B R and Hentschel M P 2013 Micro-diagnostics: X-ray and synchrotron techniques *Handbook of technical diagnostics - Fundamentals and application to structures and systems*. ed. H Czichos (Berlin, Heidelberg: Springer) pp. 287-300.
[9] Evsevleev S, Müller B R, Lange A and Kupsch A 2019 *Nucl. Instrum. Meth.* A **916** 275.
[10] Kupsch A, Lange A, Hentschel M P, Onel Y, Wolk T, Staude A, Ehrig K, Müller B R and Bruno G 2013 *J. Ceram. Sci. Tech.* **4** 169.
[11] Kupsch A, Müller B R, Lange A and Bruno G 2017 *J. Eur. Ceram. Soc*. **37** 1879
[12] Müller B R, Cooper R C, Lange A, Kupsch A, Wheeler M, Hentschel M P, Staude A, Pandey A, Shyam A and Bruno G 2018 *Acta Mater.* **144** 627.
[13] Nellesen J, Laquai R, Müller B R, Kupsch A, Hentschel M P, Anar N B, Soppa E, Tillmann W and Bruno G 2018 *J. Mater. Sci.* **53** 6021.
[14] Laquai R, Gouraud F, Müller B R, Huger M, Chotard T, Antou G and Bruno G 2019 *Materials* **12** 1017.
[15] Mack E, Laquai R, Müller B R, Helle O, Sebold D, Vaßen R and Bruno G 2019 *J. Am. Ceram. Soc*. **102** 6163.
[16] Erdmann M, Kupsch A, Müller B R, Hentschel M P, Niebergall U, Böhning M and Bruno G 2019 *J. Mater. Sci.* **54** 11739.
[17] Schob D, Roszak R, Sagradov I, Sparr H, Ziegenhorn M, Kupsch A, Léonard F, Müller B R and Bruno G 2019 *Arch. Mech*. **71** 507.
[18] Müller B R, Lange A, Harwardt M and Hentschel M P 2009 *Adv. Eng. Mater.* **11** 435.
[19] Görner W, Hentschel M P, Müller B R, Riesemeyer H, Krumrey M, Ulm G, Diete W, Klein U and Frahm R 2001 *Nucl. Instrum. Meth.* A **467-468** 703.
[20] Lange A, Hentschel M P, Kupsch A and Müller B R 2012 *Int. J. Mater. Res.* **103** 174.
[21] Al-Falahat A A M, Kupsch A, Hentschel M P, Lange A, Kardjilov N, Markötter H and Manke I 2019 *Rev. Sci. Instrum.* **90** 125108.
[22] Chapman D, Thomlinson W, Johnston R E, Washburn D, Pisano E, Gmür N, Zhong Z, Menk R, Arfelli F and Sayers D 1997 *Phys. Med. Biol.* **42** 2015.
[23] ISO 527-1:2012-06 2012 Plastics - Determination of tensile properties - Part 1: General principles (Berlin: Beuth).
[24] Puck A and Schürmann H 1998 *Compos. Sci. Technol.* **58** 1045.